ROYAL SOCIETY OPEN SCIENCE

rsos.royalsocietypublishing.org

Research

Cite this article: Huang Y, Cheng M, Xiang Z, cui Y. 2018 Facile synthesis of $NiCo_2S_4$/CNTs nanocomposites for high-performance supercapacitors. *R. Soc. open sci.* **5**: 180953.
http://dx.doi.org/10.1098/rsos.180953

Received: 19 June 2018
Accepted: 15 August 2018

Subject Category:
Chemistry

Subject Areas:
nanotechnology

Keywords:
porous $NiCo_2S_4$/CNTs, supercapacitor, different sulfide sources, cycling stability

Author for correspondence:
Yimin cui
e-mail: cuiym@buaa.edu.cn

This article has been edited by the Royal Society of Chemistry, including the commissioning, peer review process and editorial aspects up to the point of acceptance.

Electronic supplementary material is available online at https://doi.org/10.6084/m9.figshare.c.4212863.

THE ROYAL SOCIETY PUBLISHING

Facile synthesis of $NiCo_2S_4$/CNTs nanocomposites for high-performance supercapacitors

Yunxia Huang, Ming Cheng, Zhongcheng Xiang and Yimin cui

Department of Physics, Beihang University, Beijing 100191, People's Republic of China

Yc, 0000-0002-5142-7528

Herein, porous $NiCo_2S_4$/CNTs nanocomposites were synthesized via a simple hydrothermal method followed by the sulphurization process using different sulfide sources. By comparing two different sulfur sources, the samples using thioacetamide as sulfide source delivered more remarkable electrochemical performance with a high specific capacitance of 1765 F g^{-1} at 1 A g^{-1} and an admirable cycling stability with capacitance retention of 71.7% at a high current density of 10 A g^{-1} after 5000 cycles in 2 M KOH aqueous electrolyte. Furthermore, an asymmetric supercapacitor (ASC) device was successfully fabricated with the $NiCo_2S_4$/CNTs electrode as the positive electrode and graphene as the negative electrode. The device provided a maximum energy density of 29.44 W h kg^{-1} at a power density of 812 W kg^{-1}. Even at a high power density of 8006 W kg^{-1}, the energy density still reaches 16.68 W h kg^{-1}. Moreover, the ASC presents 89.8% specific capacitance retention after 5000 cycles at 5 A g^{-1}. These results reveal its great potential for supercapacitors in electrochemical energy storage field.

1. Introduction

In recent years, it is urgently needed to develop clean and renewable energy resources due to environmental pollution and depletion of fossil fuels [1–5]. Therefore, a large number of energy conversion/storage devices have been explored to meet the increasing demand for energy and power in our daily life [6–8]. Among them, supercapacitors have received considerable attention on account of their high power density, low cost, fast charge–discharge rate, and long cycling life [9–12]. Particularly, pseudocapacitors, which make use of reversible Faradaic

reactions occurring at the electrode surface to offer much higher specific capacitance, have become a research hotspot [10,13].

Transition metal oxides, hydroxides and their compounds are becoming widely explored for high-performance pseudocapacitors because of their low cost, low toxicity and great flexibility in structure and morphology [14,15]. However, their conductivity is typically too low to support fast electron transport towards high rate capability [16,17]. To overcome this problem, many substitute electrode materials have been developed. Among these substitute materials, transition metal sulfides have received considerable attention, due to their enhanced electrical conductivity and electrochemical activity compared with their corresponding transition metal oxides and hydroxides [5,18]. Transition metal sulfides, such as cobalt sulfides and nickel sulfides, have been investigated as a new electrode material for pseudocapacitors with a good performance [11,19]. Particularly, $NiCo_2S_4$ exhibited an electrical conductivity about 100 times that of $NiCo_2O_4$ and approximately 10^4 times higher than conventional mono-metal counterparts [20–22].

However, the conductivity and the structure stability of the $NiCo_2S_4$ nanomaterials reported are insufficient to meet the requirements for the high-performance supercapacitors. Many strategies have been developed to solve the above challenges, such as constructing special core shell structure [13,20,23], fabricating composite material [11,24], direct growth on conductive substrate [25,26] and so on. Among them, coupling the transition metal sulfides with carbon nanomaterials is an effective means to overcome the drawbacks. For example, carbon nanotubes (CNTs) and graphene have excellent physical properties such as electrical conductivity, large surface area and pore structure [27], which are widely used to integrate with other materials. Wen and his partners have prepared the hybrids of nickel cobalt sulfide/multi-wall carbon nanotubes ($NiCo_2S_4$/MWCNTs) by one-pot solvothermal reaction, which is able to deliver an ultrahigh specific capacitance of 2080 F g^{-1} at the current density of 1 A g^{-1} and exhibit an excellent cycling stability of 85.7% capacitance retention after 5000 cycles at 4 A g^{-1} in an asymmetric supercapacitor [24]; Yang and her cooperators have fabricated edge site-enriched nickel-cobalt sulfide (Ni-Co-S) nanoparticles anchored on graphene frameworks exhibiting a superior rate capability of 96% with the current density increased [28]. Though lots of achievements have been obtained, more effort is still needed to realize our desired high performance for energy storage material. So far, there is little literature to compare the structures and properties of the $NiCo_2S_4$ samples using the different sulfur sources under the same experimental conditions.

In this work, we successfully synthesized $NiCo_2S_4$/CNTs nanocomposites through a hydrothermal method with subsequent sulphurizing process. Meanwhile, we investigated the effect of different sulfide sources on the morphology, structure and performance of final samples. Benefiting from the unique porous structure and compositions, the sample, which was prepared with thioacetamide (TAA) as a sulfide source, showed high specific capacitance and excellent cycling stability. Furthermore, an asymmetric supercapacitor (ASC) was assembled with the $NiCo_2S_4$/CNTs electrode as a positive electrode and graphene as a negative electrode. The device delivered a high energy density of 29.44 W h kg^{-1} at a power density of 812 W kg^{-1}. The above results imply that $NiCo_2S_4$/CNTs nanocomposites are a promising electrode material in supercapacitors for practical application.

2. Material and methods

2.1. Preparation of nickel cobalt oxide nanostructures

All the chemicals were directly used after purchase without further purification. In a typical process, 0.952 g of $CoCl_2{\cdot}6H_2O$, 0.476 g of $NiCl_2{\cdot}6H_2O$, 0.37 g of NH_4F and 44 mg of CNTs were dissolved in 50 ml of deionized (DI) water and 20 ml of alcohol, resulting in homogeneous black solution under vigorous magnetic stirring and ultra-sonication for 20 min. Then, 1.5 g of hexamethylenetetramine (HMT) was added into the black solution and stirred for about 30 min. The mixed solution was transferred into a 100 ml Teflon-lined stainless steel autoclave, which was kept at 95°C for 24 h. After cooling to room temperature, the products were collected by centrifugation and washed with deionized water (DI) several times to remove the residual reactants. The obtained precipitates were dried in a vacuum oven at 60°C for 12 h.

2.2. Preparation of nickel cobalt sulfide nanostructures

93 mg of the precursors prepared in the first step and 0.2 M TAA or 0.2 M $Na_2S{\cdot}9H_2O$ were dispersed directly into 12 ml deionized water. Then, the mixed solution was added into a 25 ml Teflon-lined

stainless steel autoclave after stirring for about 30 min. Typically, the autoclave was kept at 120°C for 6 h. After cooling to room temperature, the products were collected by centrifugation and washed with DI water several times and dried at 60°C for 24 h. The resulting samples were labelled S1 and S2. The pure $NiCo_2S_4$ was also prepared by the same method except adding the CNTs. The resulting samples were labelled $NiCo_2S_4$-1 and $NiCo_2S_4$-2.

2.3. Materials characterizations

The morphologies and structures of the as-obtained samples were characterized by field emission scanning electron microscopy (FE-SEM, Hitachi S-4800), transmission electron microscopy (TEM, Hitachi JEM-2200FS), powder X-ray diffraction (XRD, Ultima IV, Cu Kα radiation) and X-ray photoelectron spectroscopy (XPS, ESCALAB 250Xi, Al Kα radiation). Nitrogen adsorption and desorption measurements were performed on Quadrasorb SI. The specific surface area was calculated using Brunauer–Emmett–Teller (BET) method.

2.4. Electrochemical measurements

All electrochemical measurements were performed on an electrochemical workstation (CHI 660D, Shanghai, China) in three-electrode configurations with 2 M KOH aqueous electrolyte. For the preparation of the working electrodes, the as-synthesized active materials were mixed with acetylene black and polyvinylidene fluoride (PVDF) with a mass ratio of 7 : 2 : 1 in N-methyl-2-pyrrolidinone. Then the mixture was coated into the nickel foam (NF) electrodes. After that, the electrodes were dried in an oven at 80°C for 12 h. The dried electrodes were then pressed using a hydraulic press at a pressure of 10 MPa as the working electrodes. The mass loadings of S1 and S2 are about 3.08 mg cm^{-2} and 3.71 mg cm^{-2}, respectively. In the three-electrode electrochemical cell, a Pt wire and a Hg/HgO electrode were used as the counter and reference electrodes, respectively. The capacitive performance of the electrodes was evaluated by cyclic voltammetry (CV), chronopotentiometry (CP) and electrochemical impedance spectroscopy (EIS). EIS measurements were carried out using this apparatus over a frequency range of 10 kHz to 0.01 Hz at 0 V with an AC amplitude of 5 mV.

For the CV measurements, the specific capacitance can be calculated according to the following equation:

$$C = \frac{\int I\mathrm{d}V}{2mV\Delta V},$$

where m is the mass of the active materials (g), V is the scan rate of the CV curves (V s^{-1}), ΔV is the potential window (V), I is the discharge current (A) and $\int I\mathrm{d}V$ is the area of one CV loop.

For the CP measurements, the specific capacitance can be calculated according to the following equation:

$$C = \frac{I\Delta t}{m\Delta V},$$

where I is the discharge current (A), Δt is the discharge time (s), m is the mass of the electrode materials (g) and ΔV is the potential range (V).

3. Results and discussion

3.1. Sample characterization

The crystal structure and phase of the samples were characterized by XRD. Figure 1 illustrates the XRD patterns of the S1 and the S2 samples. Obviously, the diffraction peaks about at 16.3°, 26.8°, 31.6°, 38.3°, 47.4°, 50.5° and 55.3° of the two samples can be indexed to the (111), (220), (311), (400), (422), (511) and (440) planes of the cubic phase of $NiCo_2S_4$ (JCPDS no. 20-0782), respectively. The XRD pattern of the S1 sample without any impurity phases indicates that the precursor was completely vulcanized into $NiCo_2S_4$. However, some additional peaks of the S2 sample at 18.4° correspond to NiS (JCPDS no. 02-1443), and the peaks at 29.8° and 51.9° for the two samples can be attributed to Co_9S_8 (JCPDS no. 02-1459), on account of the incomplete sulphurization of the S2 sample using Na_2S as sulfur source [29]. It is clear that the peaks of S1 and the S2 were similar which only had slight shifts and changes.

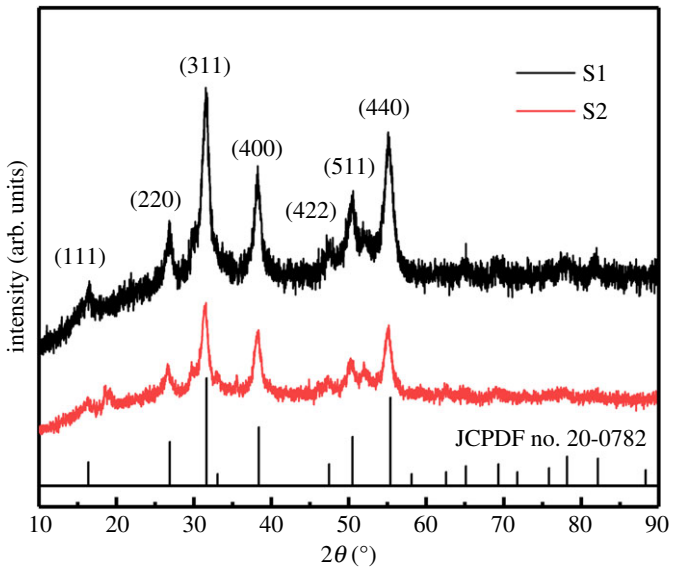

Figure 1. XRD patterns of the S1 and the S2 samples.

Furthermore, the diffraction peaks of the CNTs could not be clearly identified due to their low content and small atomic number [11].

The elemental compositions and chemical bonding states of the $NiCo_2S_4$ were further investigated by X-ray photoelectron spectroscopy (XPS). As shown in the figure 2, the elements of Ni, Co and S were clearly exhibited. For both the two samples, Co 2p and Ni 2p spectra can both be fitted with two spin–orbit peaks and two shake-up satellites (marked as 'Sat.') using the Gaussian fitting method. For Co 2p of the S1 sample (figure 2*a*), the binding energies at around 778.2 and 793.2 eV indicate the existence of Co^{3+}, while the peaks at around 780.2 and 796.01 eV are assigned to Co^{2+}. Likewise, two kinds of Ni species can be observed (figure 2*b*); the fitting peaks at 852.8 and 870.2 eV imply the characteristic of Ni^{2+}, where the binding energies at 855.6 and 873.9 eV are indexed to Ni^{3+}. These results agree with the literature of the Co 2p and Ni 2p spectra in $NiCo_2S_4$ [11,29]. Moreover, the peak (figure 2*c*) at 161.2 eV is indexed to S $2p_{3/2}$ associated with the characteristic of metal–sulfur bonds, while the peak at 162.4 eV corresponding to S $2p_{1/2}$ may be attributed to S^{2-} in low coordination at the surface, which is generally related to sulfur vacancies [25,29,30]. The similar results of the S2 sample can also be observed [31,32]. Moreover, the XPS results coincide well with the XRD results.

The morphologies and nanostructures of the samples were examined via scanning electron microscopy (SEM), as shown in figure 3. The morphologies of the predecessors are many nanosheets and the flower-like balls composed of nanosheets (figure 3*a*). No matter whether the sulfur sources are TAA (figure 3*c*,*d*) or $Na_2S \cdot 9H_2O$ (figure 3*e*,*f*), the morphology of the $NiCo_2S_4$ structures was well inherited from the precursor after the subsequent sulphuration. Obviously, the difference between the two sulfide products was the surface of the nanosheets. The surface of the S1 samples (electronic supplementary material, figure S6a) was loose and porous compared with S2 (electronic supplementary material, figure S6b). This result was also proved by the pure $NiCo_2S_4$-1 and $NiCo_2S_4$-2 (electronic supplementary material, figure S1). The porosity favours to expose richer redox sites and the electrolyte transport, which can highly facilitate rapid redox reactions and increase the contact area between the electrode and electrolytes for the effective utilization of the active materials [33–35]. Comparing figure 3 with electronic supplementary material, figure S1, it is seen that the morphologies of samples are composed of thick nanoplates without CNTs. It is obvious that adding CNTs can shrink the thickness of nanoplates to form thin nanosheets.

The nanostructures of $NiCo_2S_4$ flower-like balls were further observed by FE-TEM. The morphology of the nanosheets (figure 4*a*,*c*) was also well inherited from the precursor. Nevertheless, the sample prepared by using TAA as a sulfide source possesses more porous structures, which could provide more active sites and lead to superior electrochemical performance, consistent with the results of the SEM. From 4*a* and 4*c*, it is clear that CNTs can coat well on the surface of nanosheets, indicating that CNTs have played a part in the formation of flower-like balls, acted as a backbone matrix to uphold the structural integrity of the network and played a role as

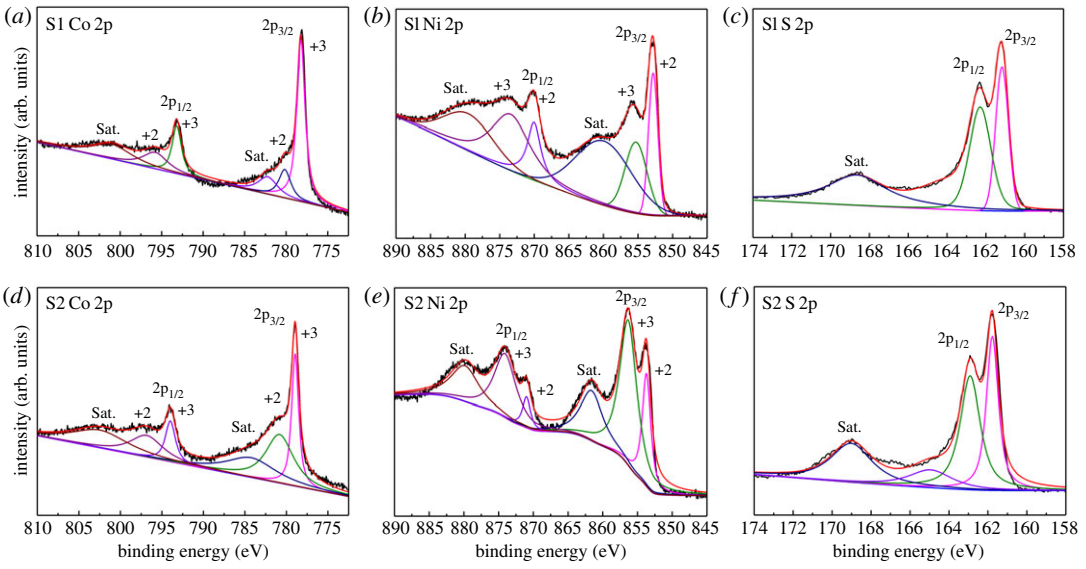

Figure 2. XPS spectra for the (*a*) Co 2p, (*b*) Ni 2p, and (*c*) S 2p for the S1 samples. XPS spectra for the (*d*) Co 2p, (*e*) Ni 2p, and (*f*) S 2p for the S2 samples.

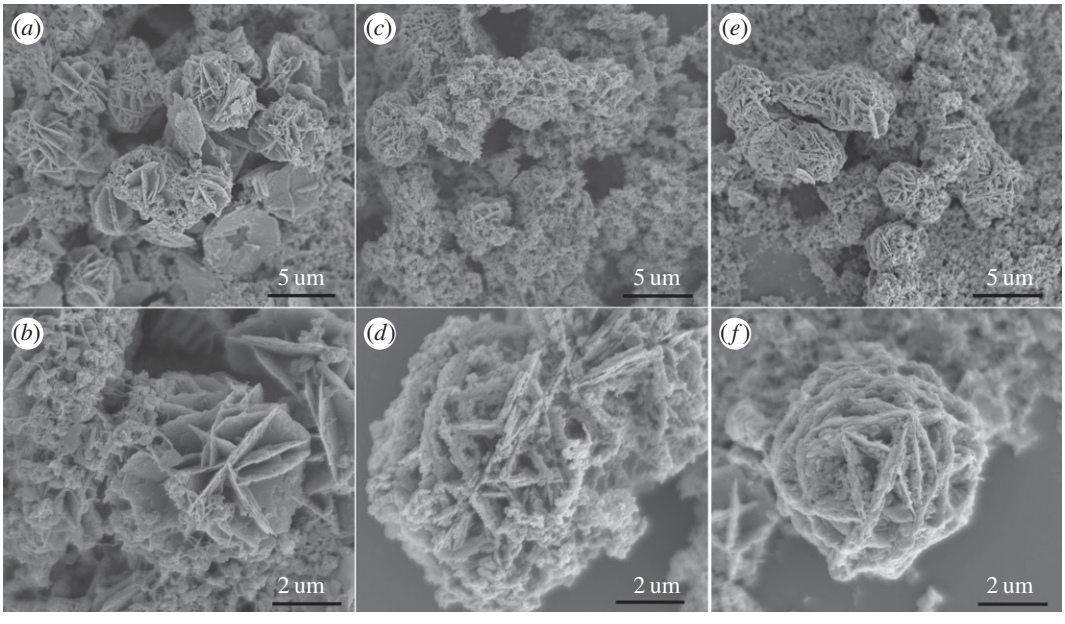

Figure 3. SEM images of the precursors (*a,b*), S1 (*c,d*) and S2 (*e,f*) at low (*a,c,e*) and high (*b,d,f*) magnifications.

electron channels [36]. In figure 4*b*, the interplanar spacing between the lattice fringe is measured to be 0.283 nm corresponding to the (311) plane of the $NiCo_2S_4$ and the corresponding fast Fourier transform (FFT) pattern (inset in figure 4*b*) confirms its good crystallinity. In figure 4*d*, the measured interplanar spacing of 0.234 nm can be indexed to the (400) plane of the $NiCo_2S_4$, and the corresponding FFT pattern (inset in figure 4*d*) also confirms its good crystallinity. These results are in good agreement with the XRD results (figure 1).

The specific surface area (SSA) and the distribution of the pore size of the electrode materials can be the judgements of the electrochemical performances. S1 and S2 samples were explored by recording the adsorption–desorption isotherms of nitrogen at 77 K. As shown in electronic supplementary material, figure S2, the SSA of S1 and S2 by using the BET method are calculated to be about 32.82 and 19.7 $m^2\,g^{-1}$, respectively. The large SSA is beneficial for substantial contact between the electrolyte and the active material, which can improve the electrochemical performances.

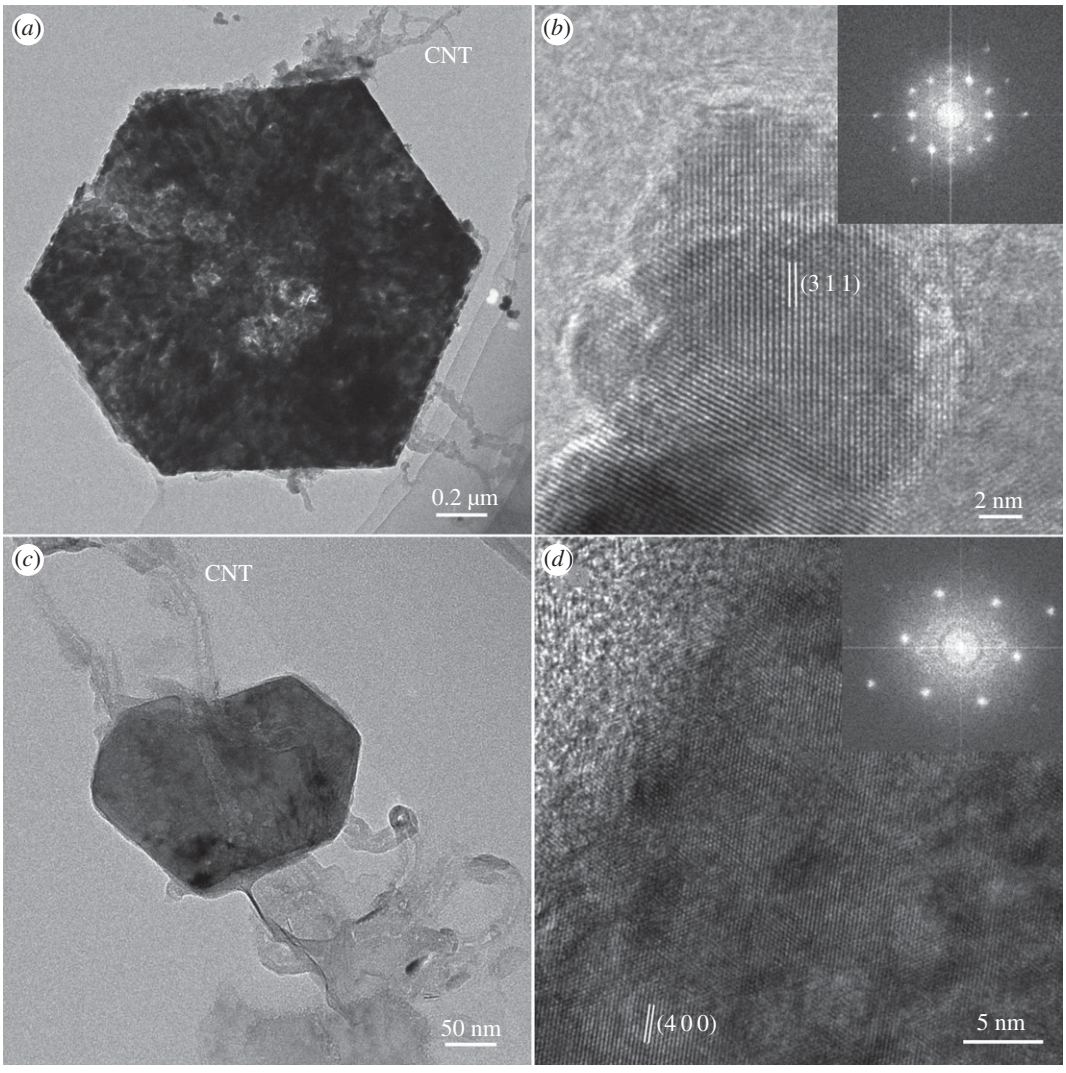

Figure 4. (*a*) and (*b*) TEM and HRTEM images of S1; the inset of (*b*) is the corresponding FFT. (*c*) and (*d*) TEM and HRTEM images of S2; the inset of (*d*) is the corresponding FFT image.

3.2. Electrochemical properties

In order to characterize the capacitor behaviour of electrode materials, the electrochemical performances of the as-synthesized samples as a positive electrode were investigated in a three-electrode system. The S1 and S2 electrodes were tested under the same conditions for comparison. Figure 5*a* compares the CV curves of the S1 with S2 electrodes obtained at a scan rate of 1 mV s^{-1}. Obviously, the integrated area covered by the CV curves of the S1 sample was much larger than the S2 sample, suggesting that the S1 sample has a superior electrochemical performance. The higher pseudocapacitive performance can be attributed to the loose and porous surface, which is conducive to the contact between the electrode and electrolytes.

Figure 5*b* compares the Galvanostatic discharge curves of the S1 and S2 electrodes at the same current density of 1 A g^{-1}. The discharging time for the S1 (971 s) is much higher than the S2 (619.6 s), which also demonstrates that the S1 sample has higher electrochemical performance. To confirm the importance of CNTs, the CV curves and Galvanostatic discharge curves of the pure $NiCo_2S_4$-1 (514.6 s) and the pure $NiCo_2S_4$-2 (402.7 s) electrodes were also measured at 1 mV s^{-1} and 1 A g^{-1} as a contrast (electronic supplementary material, figure S3). The results reveal that the samples with CNTs have better electrochemical performance than samples without CNTs. In the meantime, it is also concluded that using TAA as the sulfur source can have a better electrochemical performance than $Na_2S{\cdot}9H_2O$ as sulfur source.

The energy storage of the $NiCo_2S_4$ electrode is ascribed to the Faradaic redox reactions of $NiCo_2S_4$ in 2 M KOH electrolyte. Figure 5*c* shows cyclic voltammetry (CV) curves of the S1 electrode at various scan

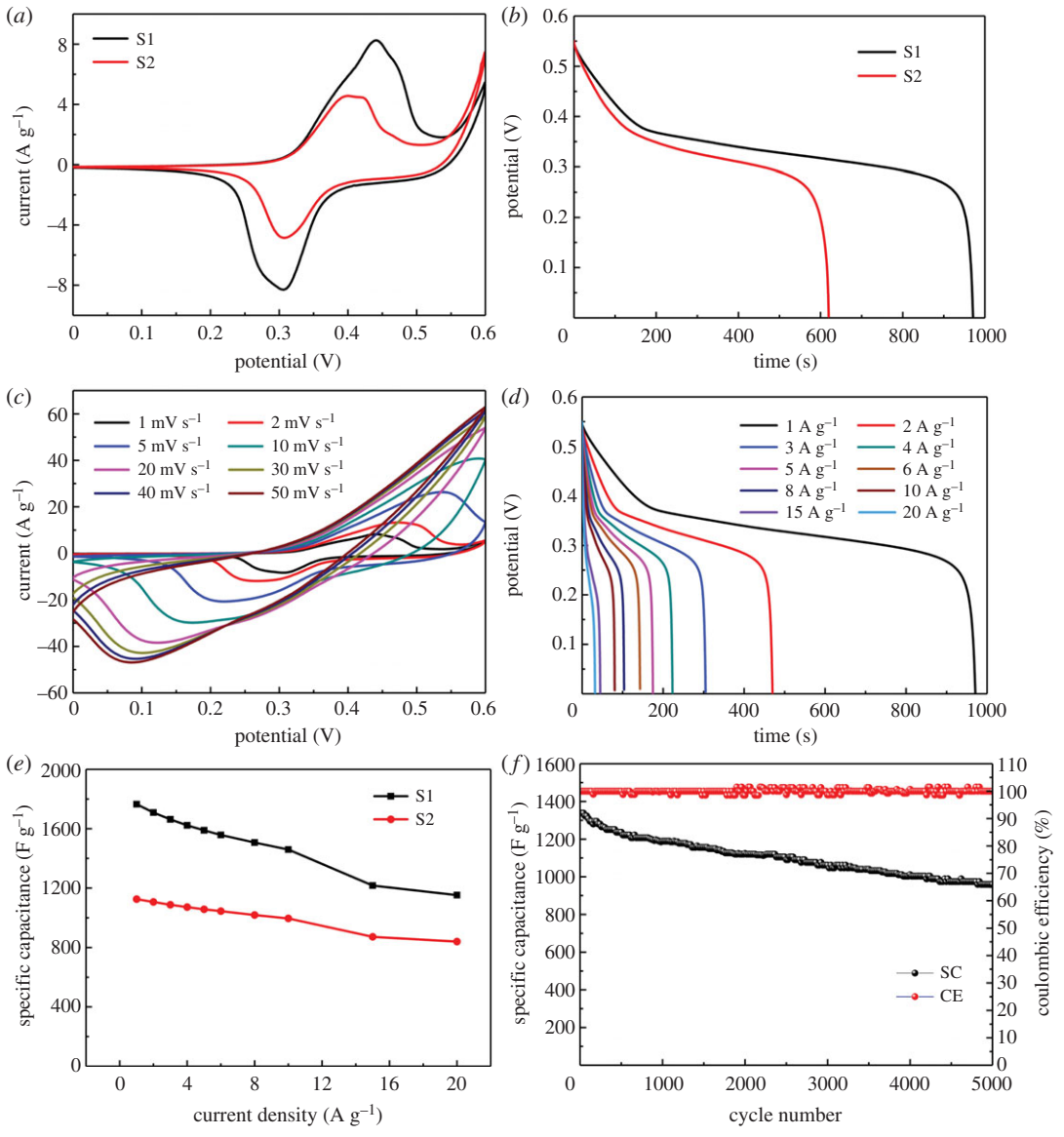

Figure 5. (*a,b*) CV curves and Galvanostatic discharge curves of the S1 and S2 electrodes measured at 1 mV s^{-1} and 1 A g^{-1}. (*c*) CV curves of the S1 electrodes at different scan rates and (*d*) Galvanostatic discharge curves at various current densities. (*e*) The specific capacitance versus current density for the S1 and S2 electrodes. (*f*) Cycling performance and coulombic efficiency of the prepared S1 electrodes over 5000 charge–discharge cycles at a constant current density of 10 A g^{-1}.

rates ranging from 1 to 50 mV s^{-1}. As the scan rate increases, the anodic and cathodic peaks move to the positive and negative potential. The obvious redox reaction peaks in the CV curves indicate that distinct pseudocapacitive characteristics of the electrode materials are mainly governed by Faradaic redox reactions, which can be originated from reversible redox processes of Ni^{2+}/Ni^{3+} and $Co^{2+}/Co^{3+}/Co^{4+}$ [29,37]. The plausible electrochemical reactions are described as follows:

$$NiCo_2S_4 + OH^- + H_2O \leftrightarrow NiSOH + 2CoSOH + 2e^-$$

$$CoSOH + OH^- \leftrightarrow CoSO + H_2O + e^-$$

Figure 5*d* further investigates the discharge times of the S1 samples at current densities from 1 to 20 A g^{-1}. According to the curves, the specific capacitances of the S1 electrodes are 1765, 1709, 1663, 1623, 1589, 1558, 1507, 1460, 1217 and 1153 F g^{-1} at the current densities of 1, 2, 3, 4, 5, 6, 8, 10, 15 and 20 A g^{-1}, respectively. Moreover, the capacitance at 10 A g^{-1} corresponds to 82.7% retention relative to 1 A g^{-1}. Figure 5*e* shows the corresponding specific capacitances versus discharge current density of the S1 and S2 electrode. Apparently, the S1 demonstrates the higher specific capacitance than the S2. Meanwhile, the results reveal that the specific capacitance decreases as the current

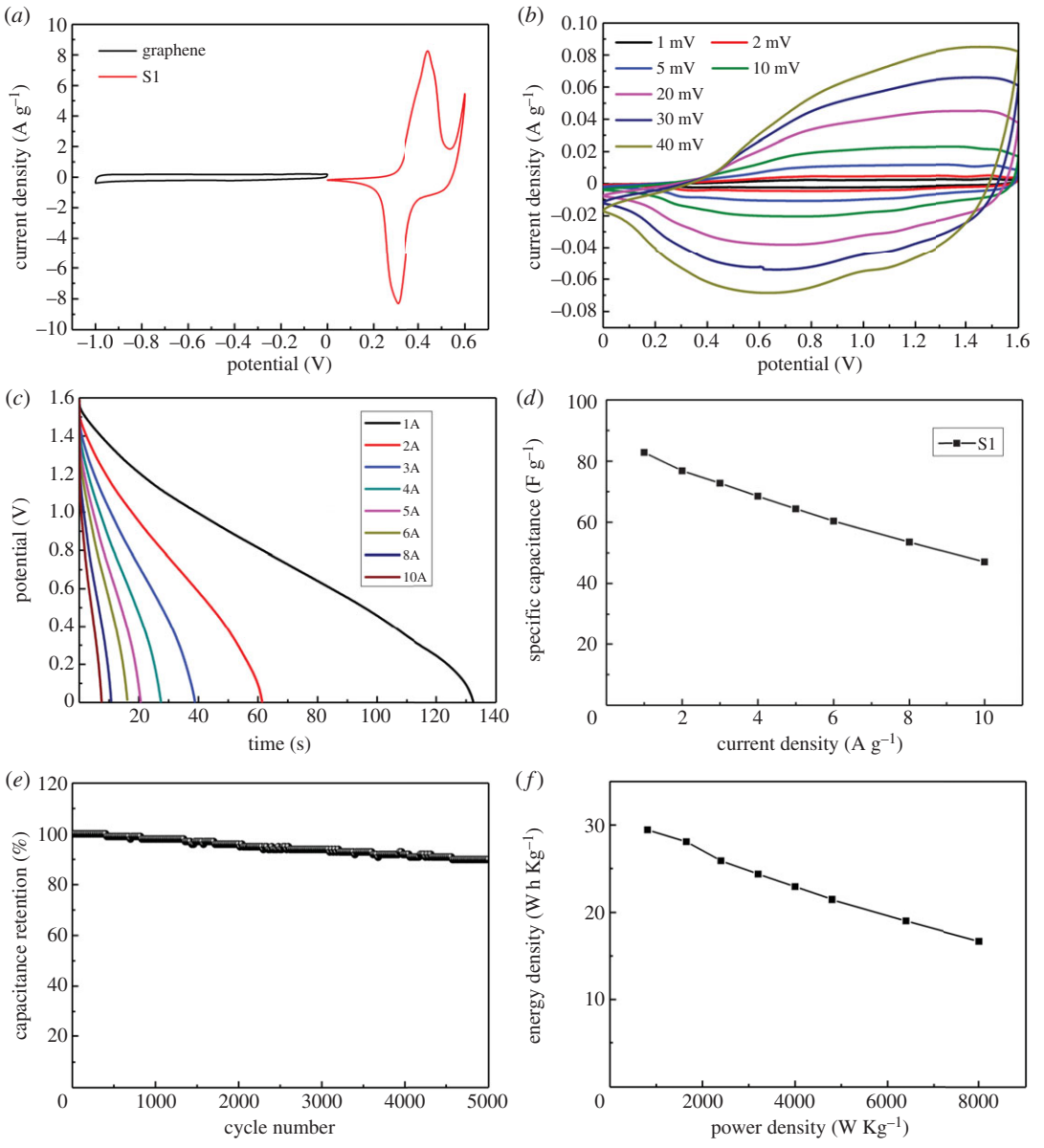

Figure 6. (*a*) CV curves of the graphene electrode and the S1 electrode at 1 mV s^{-1}. (*b*) CV curves of the S1//graphene ASC measured at different scan rate in the potential window of 0–1.6 V. (*c*) Galvanostatic discharge curves of the S1//graphene ASC at different current densities. (*d*) The specific capacitance of the S1//graphene ASC at different current densities. (*e*) Cycling stability of the S1//graphene ASC at a constant current density of 5 A g^{-1}. (*f*) Ragone plot of the S1//graphene ASC from the Galvanostatic charge–discharge curves.

density increases, which occurs because the redox reaction between Ni/Co cations and OH anions is a diffusion-controlled process through the electrode grain boundaries. However, at a current density of 20 A g^{-1}, the rate capability of the S2 samples was 74.6% retention, which was higher than that of S1 samples (65.3%).

To check the structural stability and corresponding coulombic efficiency of the prepared S1 electrodes, a cycling test was performed over 5000 charge–discharge cycles at a constant current density of 10 A g^{-1} (figure 5*f*). The specific capacitance remained approximately 71.7% of the initial value after 5000 charging–discharging cycles, thus showing excellent structural stability.

To further investigate the electrical conductivity of the samples, electrochemical impedance spectroscopy (EIS) was measured at an open circuit potential in the frequency range from 100 kHz to 0.01 Hz with an amplitude of 5 mV. Electronic supplementary material, figure S4 presents the Nyquist plots of the different electrodes with an enlarged view (inset). All the curves consist of the intersection on the real axis related to the internal resistances of the electrode (Rs), the semicircle corresponding to the charge transfer resistance (Rct) at a high frequency, and the linear slope meaning the diffusive

resistance of the capacitor behaviour at a low frequency [38]. Obviously, the Nyquist plots of the two samples present semicircles with a small diameter in a high frequency range, indicating low charge-transfer resistance. From the point intersecting with the real axis, the internal resistances of samples were approximately 0.59 and 0.71 Ω. As the previous revealed, it is notable that the trend of conductivity is well consistent with the capacitance, which can imply that there is a strong correlation between the electrical conductivity and the specific capacitance. The results demonstrate that the S1 samples can provide a better supercapacitive performance.

To further explore the potential practical application of the S1 electrodes in the energy field, an asymmetric supercapacitors (ASC) device was successfully fabricated with the S1 electrode as the positive electrode and graphene as the negative electrode in 2 M KOH electrolyte. With the discovery of graphene, it is well known that graphene (electronic supplementary material, figure S5) is an ideal supercapacitor electrode material because of its high specific surface area, good conductivity and excellent electrochemical stability. The mass loading of graphene is determined by balancing the charge between both electrodes. Figure 6*a* presents the CV curves of the graphene electrode and the S1 electrode at 1 mV s^{-1}. The CV curves of the graphene exhibit a nearly rectangular shape without redox peaks, which imply the excellent EDLC performance with a potential window from −1.0 to 0 V. As for S1 electrode in the voltage window from 0 to 0.6 V, two pairs of redox peaks are observed, owing to the classic pseudocapacitance. According to the previous researches, we calculated the optimal mass ratio m (S1)/m (graphene) ≈0.2 based on their specific capacitances and potential windows, which can obtain the maximum capacitance of the device and meet the requirement of the charge balance between both electrodes.

Figure 6*b* shows CV curves of S1//graphene in a voltage window of 0–1.6 V at different scan rates in a 2 M KOH electrolyte. The ASC curves show a quasi-rectangular shape with redox peaks, indicating that the whole capacitance can be attributed to the combination of ELDC and Faradaic pseudocapacitance. The capacitances calculated based on the CV curves show that the ASC provides a high capacitance of 100 F g^{-1} at 1 mV s^{-1} scan rate and still exhibits 80 F g^{-1} at a high scan rate of 50 mV s^{-1}. The capacitance drop is generally caused by the insufficient time for the electrolyte to access the electrode surface.

Figure 6*c* presents the Galvanostatic charge–discharge measurements at various current densities from 1 to 10 A g^{-1} in the potential window of 1.6 V. The ASC exhibits a high specific capacitance of 82.8 F g^{-1} at the current density of 1 A g^{-1}. With the current density increasing to 10 A g^{-1}, the specific capacitance still remains 46.9 F g^{-1}, which is 56.6% of the capacitance retained. The cycle stability of the ASC device was valued by the GCD measurements at a high current density of 5 A g^{-1} for 5000 cycles (figure 6*e*). Remarkably, only 10.2% capacity decay is observed after 5000 cycles.

Another essential factor to demonstrate the electrochemical performance of devices is energy density. Figure 6*f* presents the Ragone plot of the ASC from the Galvanostatic charge–discharge curves. The ASC achieved a high energy density of 29.44 W h kg^{-1} at a power density of 812 W kg^{-1} and can retain 16.68 W h kg^{-1} at a higher power density of 8006 W kg^{-1}. This high energy density may be attributed to its high specific capacitance and the good match of $NiCo_2S_4$/CNTS with graphene. The above results indicate that the $NiCo_2S_4$/CNTS is a promising candidate material in supercapacitors field.

4. Conclusion

In summary, we have successfully synthesized $NiCo_2S_4$/CNTS nanocomposites via a simple hydrothermal method with subsequent sulphurizing process. By comparing two different sulfur sources, the S1 sample using TAA as sulfur source possesses more pure phase and exhibits a higher capacitance of 1765 F g^{-1} than S2 electrodes with 1250 F g^{-1} at a current density of 1 A g^{-1}, which might be attributed to its loose and porous structure. Moreover, an ASC device based on $NiCo_2S_4$/CNTS as the positive electrode and graphene as the negative electrode has been assembled. It achieved a high specific capacitance of 82.8 F g^{-1} at a current density of 1 A g^{-1} with a potential window of 1.6 V. Furthermore, it can deliver a remarkable energy density of 29.44 W h kg^{-1} at a power density of 812 W kg^{-1}. Additionally, the ASC device exhibits good cycling stability (89.8% retaining after 5000 cycles). This study indicates their potential as a promising candidate material for high-performance supercapacitors.

Ethics. This research did not include animals and humans.

Data accessibility. We have deposited our data in the Dryad Digital Repository (http://dx.doi.org/10.5061/dryad.nf1kf60) [39]. The datasets supporting this article have been uploaded as part of the electronic supplementary material.

Authors' contributions. Y.H. designed and synthesized the samples. Y.H. and Y.c. wrote the manuscript. M.C. and Z.X. participated in analysing the characterization results and made many suggestions. M.C. coordinated the study and revised the manuscript. All authors gave final approval for publication.

Competing interests. The authors declare no conflict of interest.

Funding. This work was supported by the National Natural Science Foundation of China (no. 51571006).

Acknowledgements. We thank Xinran Zhang and Hongsheng Fan for the help in TEM.

References

1. Tang YF, Liu ZY, Guo WF, Chen T, Qiao YQ, Mu SC, Zhao YF, Gao FM. 2016 Honeycomb-like mesoporous cobalt nickel phosphate nanospheres as novel materials for high performance supercapacitor. *Electrochim. Acta* **190**, 118–125. (doi:10.1016/j.electacta.2016.01.042)
2. Yang XJ, Sun HM, Zan P, Zhao LJ, Lian JS. 2016 Growth of vertically aligned $Co_3S_4/CoMo_2S_4$ ultrathin nanosheets on reduced graphene oxide as a high-performance supercapacitor electrode. *J. Mater. Chem. A* **4**, 18 857–18 867. (doi:10.1039/c6ta07898b)
3. Liu SD *et al.* 2017 Controllable sulfuration engineered NiO nanosheets with enhanced capacitance for high rate supercapacitors. *J. Mater. Chem. A* **5**, 4543–4549. (doi:10.1039/c6ta11049e)
4. Huang YY, Shi TL, Jiang SL, Cheng SY, Tao XX, Zhong Y, Liao GL, Tang ZR. 2016 Enhanced cycling stability of $NiCo_2S_4$@NiO core-shell nanowire arrays for all-solid-state asymmetric supercapacitors. *Sci. Rep.* **6**, 38620. (doi:10.1038/srep38620)
5. Wen YX *et al.* 2017 Facile synthesis of ultrathin $NiCo_2S_4$ nano-petals inspired by blooming buds for high-performance supercapacitors. *J. Mater. Chem. A* **5**, 7144–7152. (doi:10.1039/c7ta01326d)
6. Guo M, Balamurugan J, Thanh TD, Kim NH, Lee JH. 2016 Facile fabrication of Co_2CuS_4 nanoparticle anchored N-doped graphene for high-performance asymmetric supercapacitors. *J. Mater. Chem. A* **4**, 17 560–17 571. (doi:10.1039/c6ta07400f)
7. Guan BY, Yu Y, Wang X, Song SY, Lou XW. 2017 Formation of onion-like $NiCo_2S_4$ particles via sequential ion-exchange for hybrid supercapacitors. *Adv. Mater.* **29**, 1605051. (doi:10.1002/adma.201605051)
8. Wu ZB, Pu XL, Ji XB, Zhu YR, Jing MJ, Chen QY, Jiao FP. 2015 High energy density asymmetric supercapacitors from mesoporous $NiCo_2S_4$ nanosheets. *Electrochim. Acta* **174**, 238–245. (doi:10.1016/j.electacta.2015.06.011)
9. Zhu YR, Wu ZB, Jing MJ, Yang XM, Song WX, Ji XB. 2015 Mesoporous $NiCo_2S_4$ nanoparticles as high-performance electrode materials for supercapacitors. *J. Power Sources* **273**, 584–590. (doi:10.1016/j.jpowsour.2014.09.144)
10. Chen JW, Wang X, Wang JX, Lee PS. 2016 Sulfidation of NiMn-layered double hydroxides/graphene oxide composites toward supercapacitor electrodes with enhanced performance. *Adv. Energy Mater.* **6**, 1501745. (doi:10.1002/aenm.201501745)
11. Li DL, Gong YN, Pan CX. 2016 Facile synthesis of hybrid CNTs/$NiCo_2S_4$ composite for high performance supercapacitors. *Sci. Rep.* **6**, 7. (doi:10.1038/srep29788)
12. Lu Y, Zhang ZW, Liu XM, Wang WX, Peng T, Guo PF, Sun HB, Yan HL, Luo YS. 2016 $NiCo_2S_4$/carbon nanotube nanocomposites with a chain-like architecture for enhanced supercapacitor performance. *CrystEngComm* **18**, 7696–7706. (doi:10.1039/c6ce01556e)
13. Li R, Wang SL, Huang ZC, Lu FX, He TB. 2016 $NiCo_2S_4$@$Co(OH)_2$ core-shell nanotube arrays in situ grown on Ni foam for high performances asymmetric supercapacitors. *J. Power Sources* **312**, 156–164. (doi:10.1016/j.jpowsour.2016.02.047)
14. Yan ML, Yao YD, Wen JQ, Long L, Kong ML, Zhang GG, Liao XM, Yin GF, Huang ZB. 2016 Construction of a hierarchical $NiCo_2S_4$@PPy core shell heterostructure nanotube array on Ni foam for a high-performance asymmetric supercapacitor. *ACS Appl. Mater. Interfaces* **8**, 24 525–24 535. (doi:10.1021/acsami.6b05618)
15. Cheng M, Duan SB, Fan HS, Su XR, Cui YM, Wang RM. 2017 Core@shell CoO@Co_3O_4 nanocrystals assembling mesoporous microspheres for high performance asymmetric supercapacitors. *Chem. Eng. J.* **327**, 100–108. (doi:10.1016/j.cej.2017.06.042)
16. Zhu J, Tang SC, Wu J, Shi XL, Zhu BG, Meng XK. 2017 Wearable high-performance supercapacitors based on silver-sputtered textiles with $FeCo_2S_4$-$NiCo_2S_4$ composite nanotube-built multitripod architectures as advanced flexible electrodes. *Adv. Energy Mater.* **7**, 1601234. (doi:10.1002/aenm.201601234)
17. Abureden S, Hassan FM, Lui G, Sy S, Batmaz R, Ahn W, Yu AP, Chen ZW. 2017 Modified chalcogens with a tuned nano-architecture for high energy density and long life hybrid super capacitors. *J. Mater. Chem. A* **5**, 7523–7532. (doi:10.1039/c7ta00897j)
18. Liu XB, Wu ZP, Yin YH. 2017 Hierarchical $NiCo_2S_4$@PANI core/shell nanowires grown on carbon fiber with enhanced electrochemical performance for hybrid supercapacitors. *Chem. Eng. J.* **323**, 330–339. (doi:10.1016/j.cej.2017.04.115)
19. Zhu YR, Huang ZD, Hu ZL, Xi LJ, Ji XB, Liu Y. 2018 3D interconnected ultrathin cobalt selenide nanosheets as cathode materials for hybrid supercapacitors. *Electrochim. Acta* **269**, 30–37. (doi:10.1016/j.electacta.2018.02.146)
20. Peng TQ, Yi H, Sun P, Jing Y, Wang RJ, Wang HW, Wang XF. 2016 In situ growth of binder-free CNTs@Ni-Co-S nanosheets core/shell hybrids on Ni mesh for high energy density asymmetric supercapacitors. *J. Mater. Chem. A* **4**, 8888–8897. (doi:10.1039/c6ta02410f)
21. Wu X, Li S, Wang B, Liu J, Yu M. 2017 In situ template synthesis of hollow nanospheres assembled from $NiCo_2S_4$@C ultrathin nanosheets with high electrochemical activities for lithium storage and ORR catalysis. *Phys. Chem. Chem. Phys.* **19**, 11 554–11 562. (doi:10.1039/c7cp00509a)
22. Chen HC, Jiang JJ, Zhang L, Wan HZ, Qi T, Xia DD. 2013 Highly conductive $NiCo_2S_4$ urchin-like nanostructures for high-rate pseudocapacitors. *Nanoscale* **5**, 8879–8883. (doi:10.1039/c3nr02958a)
23. Yang YF, Cheng D, Chen SJ, Guan YL, Xiong J. 2016 Construction of hierarchical $NiCo_2S_4$@$Ni(OH)_2$ core-shell hybrid nanosheet arrays on Ni foam for high-performance aqueous hybrid supercapacitors. *Electrochim. Acta* **193**, 116–127. (doi:10.1016/j.electacta.2016.02.053)
24. Wen P, Fan MJ, Yang DS, Wang Y, Cheng HL, Wang JQ. 2016 An asymmetric supercapacitor with ultrahigh energy density based on nickle cobalt sulfide nanocluster anchoring multi-wall carbon nanotubes hybrid. *J. Power Sources* **320**, 28–36. (doi:10.1016/j.jpowsour.2016.04.066)
25. Ma LB *et al.* 2016 Self-assembled ultrathin $NiCo_2S_4$ nanoflakes grown on Ni foam as high-performance flexible electrodes for hydrogen evolution reaction in alkaline solution. *Nano Energy* **24**, 139–147. (doi:10.1016/j.nanoen.2016.04.024)
26. Hao L, Shen LF, Wang J, Xu YL, Zhang XG. 2016 Hollow $NiCo_2S_4$ nanotube arrays grown on carbon textile as a self-supported electrode for asymmetric supercapacitors. *RSC Adv.* **6**, 9950–9957. (doi:10.1039/c5ra24068a)
27. Chen ZH, Wan ZH, Yang TZ, Zhao MG, Lv XY, Wang H, Ren XL, Mei XF. 2016 Preparation of nickel cobalt sulfide hollow nanocolloids with enhanced electrochemical property for supercapacitors application. *Sci. Rep.* **6**, 25151. (doi:10.1038/srep25151)
28. Yang J, Yu C, Fan XM, Liang SX, Li SF, Huang HW, Ling Z, Hao C, Qiu JS. 2016 Electroactive edge site-enriched nickel-cobalt sulfide into graphene frameworks for high-performance asymmetric supercapacitors. *Energy Environ. Sci.* **9**, 1299–1307. (doi:10.1039/c5ee03633j)
29. Chen XJ, Chen D, Guo XY, Wang RM, Zhang HZ. 2017 Facile growth of caterpillar-like NiCo2S4 nanocrystal arrays on nickle foam for high-performance supercapacitors. *ACS Appl. Mater. Interfaces.* **9**, 18 774–18 781. (doi:10.1021/acsami.7b03254)

30. Lu F *et al.* 2016 Engineering sulfur vacancies and impurities in $NiCo_2S_4$ nanostructures toward optimal supercapacitive performance. *Nano Energy* **26**, 313–323. (doi:10.1016/j.nanoen.2016.05.042)
31. Wei C, Huang Y, Xue SS, Zhang X, Chen XF, Yan J, Yao W. 2017 One-step hydrothermal synthesis of flaky attached hollow-sphere structure $NiCo_2S_4$ for electrochemical capacitor application. *Chem. Eng. J.* **317**, 873–881. (doi:10.1016/j.cej.2017.02.130)
32. Yuan DX, Huang G, Yin DM, Wang XX, Wang CL, Wang LM. 2017 Metal-organic framework template synthesis of $NiCo_2S_4$@C encapsulated in hollow nitrogen-doped carbon cubes with enhanced electrochemical performance for lithium storage. *ACS Appl. Mater. Interfaces* **9**, 18 178–18 186. (doi:10.1021/acsami.7b02176)
33. Zhu BG, Tang SC, Vongehr S, Xie H, Zhu J, Meng XK. 2016 $FeCo_2O_4$ submicron-tube arrays grown on Ni foam as high rate-capability and cycling-stability electrodes allowing superior energy and power densities with symmetric supercapacitors. *Chem. Commun.* **52**, 2624–2627. (doi:10.1039/c5cc08857g)
34. Tang SC, Zhu BG, Shi XL, Wu J, Meng XK. 2017 General controlled sulfidation toward achieving novel nanosheet-built porous square-$FeCo_2S_4$-tube arrays for high-performance asymmetric all-solid-state pseudocapacitors. *Adv. Energy Mater.* **7**, 1601985. (doi:10.1002/aenm.201601985)
35. Gao YP, Huang KJ. 2017 $NiCo_2S_4$ materials for supercapacitor applications. *Chem. Asian J.* **12**, 1969–1984. (doi:10.1002/asia.201700461)
36. Zhu YG, Wang Y, Shi YM, Wong JI, Yang HY. 2014 CoO nanoflowers woven by CNT network for high energy density flexible micro-supercapacitor. *Nano Energy* **3**, 46–54. (doi:10.1016/j.nanoen.2013.10.006)
37. Xiong XH, Waller G, Ding D, Chen DC, Rainwater B, Zhao BT, Wang ZX, Liu ML. 2015 Controlled synthesis of $NiCo_2S_4$ nanostructured arrays on carbon fiber paper for high-performance pseudocapacitors. *Nano Energy* **16**, 71–80. (doi:10.1016/j.nanoen.2015.06.018)
38. Cheng M, Fan HS, Song YJ, Cui YM, Wang RM. 2017 Interconnected hierarchical $NiCo_2S_4$ microspheres as high-performance electrode materials for supercapacitors. *Dalton Trans.* **46**, 9201–9209. (doi:10.1039/c7dt01289f)
39. Huang Y, Cheng M, Xiang Z, cui Y. 2018 Data from: Facile synthesis of $NiCo_2S_4$/CNTs nanocomposites for high-performance supercapacitors. Dryad Digital Repository. (doi:10.5061/dryad.nf1kf60)